

Absence of Long-Range Magnetic Ordering in a Trirutile High-Entropy Oxide
(Mn_{0.2}Fe_{0.2}Co_{0.2}Ni_{0.2}Cu_{0.2})Ta_{1.92}O₆

Gina Angelo,^a Liana Klivansky,^b Jeremy G. Philbrick,^c Tai Kong,^{c,d} Jian Zhang,^b Xin Gui^{a}*

^a Department of Chemistry, University of Pittsburgh, Pittsburgh, PA, 15260, USA

^b The Molecular Foundry, Lawrence Berkeley National Laboratory, Berkeley, CA, 94720, USA

^c Department of Physics, University of Arizona, Tucson, AZ, 85721, USA

^d Department of Chemistry and Biochemistry, University of Arizona, Tucson, AZ, 85721, USA

Abstract

Functionalities of solid-state materials are usually considered to be dependent on their crystal structures. The limited structural types observed in the emerged high-entropy oxides put constraints on exploration of their physical properties and potential applications. Herein, we synthesized the first high-entropy oxide in a trirutile structure, (Mn_{0.2}Fe_{0.2}Co_{0.2}Ni_{0.2}Cu_{0.2})Ta_{1.92}O₆, and investigated its magnetism. The phase purity and high-entropy nature were confirmed by powder X-ray diffraction and energy-dispersive spectroscopy, respectively. X-ray photoelectron spectroscopy indicated divalent Mn, Co, Ni and Cu along with trivalent Fe. Magnetic properties measurements showed antiferromagnetic coupling and potential short-range magnetic ordering below ~ 4 K. The temperature-dependent heat capacity data measured under zero and high magnetic field confirmed the lack of long-range magnetic ordering and a possible low-temperature phonon excitation. The discovery of the first trirutile high-entropy oxide opens a new way for studying the relationship between the highly disordered atomic arrangement and their magnetic interaction. Furthermore, it provides a new direction for exploring functionalities of high-entropy oxides.

Introduction

High-entropy oxides (HEOs) are a type of material where five or more elements are randomly distributed in equiatomic stoichiometry on the same atomic site. Vast applications such as catalysis¹ and reversible energy storage² were found for HEOs. Better mechanical properties and resistance to oxidation/corrosion were also observed for HEOs^{3,4}. In addition, magnetic insulating HEOs were reported due to their potential application in the next-generation memory and spintronic devices⁵. Since Rost et. al. discovered the first HEO in rocksalt structure⁶, there have been great efforts to expand the structural types of HEOs. To date, ten major crystal structures were found for HEOs: bixbyite (A_2O_3)⁷, delafossite (ABO_2)⁸, fluorite (AO_2)⁹, magnetoplumbite ($AB_{12}O_{19}$)¹⁰, mullite-type ($A_2B_4O_{10}$)¹¹, perovskite (ABO_3)¹², pyrochlore ($A_2B_2O_7$)^{13,14}, rocksalt (AO)⁶, Ruddlesden-Popper phase ($A_{n+1}B_nO_{3n+1}$)¹⁵ and spinel (AB_2O_4)¹⁶ where A and B are cations. However, many structural types remain obscure, which significantly limits the manipulation and exploration of HEOs' properties. Furthermore, research surrounding their magnetic properties is only recently studied¹⁷. Upon investigation, HEOs can possess complicated magnetic properties due to the disordering of multiple transition metals, e.g., the spin-glass states in perovskite HEOs¹⁸ and tunable magnetism in spinel HEOs¹⁶. Considering the importance of crystal structure in determining physical properties, expanding the structural families of HEOs is crucial for exploring their functionalities and potential applications.

Herein, we report the first trirutile HEO, $(Mn_{0.2}Fe_{0.2}Co_{0.2}Ni_{0.2}Cu_{0.2})Ta_{1.92}O_6$, belonging to space group $P 4_2/mnm$ (no. 136) evidenced by X-ray diffraction (XRD) and energy-dispersive spectroscopy (EDS). While there were reports of rutile HEOs¹⁹, the trirutile structure remains unfounded. Trirutile i.e. AB_2O_6 , is a derivative of the rutile structure i.e. AO_2 , wherein an additional element disrupts the repeatability of the rutile structure such that a $1 \times 1 \times 3$ superlattice is formed. $NiTa_2O_6$ ²⁰, $CuTa_2O_6$ ²¹ and $CoTa_2O_6$ ²² have all been studied for their antiferromagnetic properties as trirutile oxides and we employed $CoTa_2O_6$ as the parent compound, which was reported to be antiferromagnetically ordered below $T_N \sim 6.6$ K²². However, when doped with Mg, i.e., $Co_{1-x}Mg_xTa_2O_6$, the antiferromagnetic ground state is quenched at $x=10\%$ while a short-range ferromagnetic correlation can be found in all series of compositions²³. Considering that the theoretical calculations suggest the ferromagnetic ground state²³ competing ferromagnetic and antiferromagnetic interactions must exist in $CoTa_2O_6$. Our investigation on the physical properties

of $(\text{Mn}_{0.2}\text{Fe}_{0.2}\text{Co}_{0.2}\text{Ni}_{0.2}\text{Cu}_{0.2})\text{Ta}_{1.92}\text{O}_6$ suggests short-range antiferromagnetic interaction resulting from the highly disordered transition-metal site. Therefore, the trirutile CoTa_2O_6 provides a good platform for investigating the interplay between magnetism and the crystallographic disorder on the Co site, with further possibilities to extend the scope of physical properties in trirutile HEOs.

Experimental Details

Synthesis of $(\text{Mn}_{0.2}\text{Fe}_{0.2}\text{Co}_{0.2}\text{Ni}_{0.2}\text{Cu}_{0.2})\text{Ta}_{1.92}\text{O}_6$

$(\text{Mn}_{0.2}\text{Fe}_{0.2}\text{Co}_{0.2}\text{Ni}_{0.2}\text{Cu}_{0.2})\text{Ta}_{1.92}\text{O}_6$ was prepared by mixing CoO powder (99.995%, Thermo Scientific), MnO powder (99.99%, Thermo Scientific), CuO powder (99.7%, ~200 mesh, Alfa Aesar), NiO powder (99.998%, Thermo Scientific), Fe_2O_3 powder (99.9%, Thermo Scientific), and Ta_2O_5 powder (99.5% Thermo Scientific), and by placing the 0.2 : 0.2 : 0.2 : 0.2 : 0.1 : 0.96 mixture into an alumina crucible. The crucible was covered with a small alumina lid, placed into a larger crucible, and then surrounded with activated charcoal (untreated, ≤ 5 mm, Sigma-Aldrich). This assembly was then placed into a microwave (1000 W, Model 40GR47) in the air, equipped with firebricks for further insulation and microwaved for a total of 30 minutes at 5-minute intervals with grinding in between. The sample was then pressed into a pellet and placed in a furnace pre-heated to 1250 °C in air for 1 hr, then air quenched. The resulting sample is a homogeneous brown chunk that is stable in air. A high purity phase could not be realized without a 4% deficiency in Ta_2O_5 or microwaving, the reasons for which are detailed later.

Phase Identification:

$(\text{Mn}_{0.2}\text{Fe}_{0.2}\text{Co}_{0.2}\text{Ni}_{0.2}\text{Cu}_{0.2})\text{Ta}_{1.92}\text{O}_6$ was crushed into a powder and prepared for powder X-ray diffraction (XRD). A Bruker D2 PHASER was used with Cu K_α radiation ($\lambda = 1.54060$ Å, Ge monochromator). The Bragg angle measured was from 5 to 100 ° at a rate of 1.7 °/min with a step of 0.012 °. Rietveld fitting in FULLPROF was employed to analyze the crystal structure and test the phase purity of $(\text{Mn}_{0.2}\text{Fe}_{0.2}\text{Co}_{0.2}\text{Ni}_{0.2}\text{Cu}_{0.2})\text{Ta}_{1.92}\text{O}_6$.²⁴

Physical Properties Measurements:

Magnetic Properties were measured in a Quantum Design Dynacool physical properties measurement system (PPMS) (1.8- 300 K, 0-9 T) equipped with ACMS II with both DC and AC magnetic fields available as well as a vibrating-sample magnetometer (VSM). Heat capacity was measured in the PPMS from 1.9 K to 37 K. Resistivity measurements were conducted in the PPMS from 310 K to 350 K using the four-probe method with platinum wires attached to the representative sample using silver epoxy.

Scanning Electron Microscopy (SEM) with Energy-Dispersive Spectroscopy (EDS):

Compositional analysis was performed via scanning electron microscopy (SEM) with energy-dispersive spectroscopy (EDS). A Ziess Sigma 500 VP SEM with Oxford Aztec X-EDS was used with an electron beam energy of 20 kV.

Oxidation States Analysis:

X-ray photoelectron spectroscopy (XPS) was performed in a Thermo Scientific™ K-AlphaPlus™ instrument equipped with monochromatic Al K_{α} radiation (1486.7 eV) as the excitation source. The X-ray analysis area for measurement was set at $200 \times 400 \mu\text{m}$ (ellipse shape) and a flood gun was used for charge compensation. The pass energy was 200 eV for the wide (survey) spectra and 50 eV for the high-resolution regions (narrow spectra). The base pressure of the analysis chamber was less than $\sim 1 \times 10^{-9}$ mbar. The analysis chamber pressure was at 1×10^{-7} mbar during data acquisition. Data were collected and processed using the Thermo Scientific Avantage XPS software package.

Results and Discussion

Crystal structure and compositional analysis: Powder XRD pattern of the air-quenched sample from 5 to 100° is shown in Figure 1(a). The pattern was fitted via Rietveld method by using the crystal structure of reported CoTa_2O_6 ²⁵. The fitting parameters, i.e., $R_p = 3.62\%$, $R_{wp} = 4.63\%$, $R_{exp} = 4.02\%$ and $\chi^2 = 1.32$, showed good match between the trirutile CoTa_2O_6 and the proposed HEO $(\text{Mn}_{0.2}\text{Fe}_{0.2}\text{Co}_{0.2}\text{Ni}_{0.2}\text{Cu}_{0.2})\text{Ta}_{1.92}\text{O}_6$. No prominent secondary phase was found, indicating that $(\text{Mn}_{0.2}\text{Fe}_{0.2}\text{Co}_{0.2}\text{Ni}_{0.2}\text{Cu}_{0.2})\text{Ta}_{1.92}\text{O}_6$ crystallizes in the same space group as CoTa_2O_6 , i.e., $P4_2/mnm$ with a high purity. The refined lattice parameters of $(\text{Mn}_{0.2}\text{Fe}_{0.2}\text{Co}_{0.2}\text{Ni}_{0.2}\text{Cu}_{0.2})\text{Ta}_{1.92}\text{O}_6$ are $a = 4.73179(1) \text{ \AA}$, $c = 9.20395(3) \text{ \AA}$, which creates a slightly smaller unit cell than CoTa_2O_6 ($a = 4.73580 \text{ \AA}$, $c = 9.17080 \text{ \AA}$) with smaller tetragonality, i.e., smaller c/a ratio. The fitted atomic coordinates are shown in Table S1 in the supporting information (SI), which further confirms the trirutile structure for $(\text{Mn}_{0.2}\text{Fe}_{0.2}\text{Co}_{0.2}\text{Ni}_{0.2}\text{Cu}_{0.2})\text{Ta}_{1.92}\text{O}_6$. The obtained crystal structure is shown in Figures 1(b) & 1(c). Edge-shared M@O_6 and Ta@O_6 octahedra stack along the c axis and are connected with each other in a corner-sharing manner. The M@O_6 layers with high-entropy site consisting of $3d$ transition metals within ab plane are separated by Ta@O_6 layers.

In order to confirm the high-entropy nature of $(\text{Mn}_{0.2}\text{Fe}_{0.2}\text{Co}_{0.2}\text{Ni}_{0.2}\text{Cu}_{0.2})\text{Ta}_{1.92}\text{O}_6$, SEM-EDS analysis was performed. In two distinct regions of $(\text{Mn}_{0.2}\text{Fe}_{0.2}\text{Co}_{0.2}\text{Ni}_{0.2}\text{Cu}_{0.2})\text{Ta}_{1.92}\text{O}_6$, elemental maps were collected and can be seen in Figure 1(d), for which the results are shown in Table S2 in the supporting information. The average chemical formula was found to be $\text{Mn}_{0.19(1)}\text{Fe}_{0.20(1)}\text{Co}_{0.18(1)}\text{Ni}_{0.20(1)}\text{Cu}_{0.20(2)}\text{Ta}_{1.92(1)}\text{O}_6$. Since $(\text{Mn}_{0.2}\text{Fe}_{0.2}\text{Co}_{0.2}\text{Ni}_{0.2}\text{Cu}_{0.2})\text{Ta}_{1.92}\text{O}_6$ is an insulator (as discussed later), charging effects may affect the EDS results²⁶. When considering this, our results are within the error of loading composition. Therefore, all subsequent calculations were performed based on the loading composition, i.e., $(\text{Mn}_{0.2}\text{Fe}_{0.2}\text{Co}_{0.2}\text{Ni}_{0.2}\text{Cu}_{0.2})\text{Ta}_{1.92}\text{O}_6$.

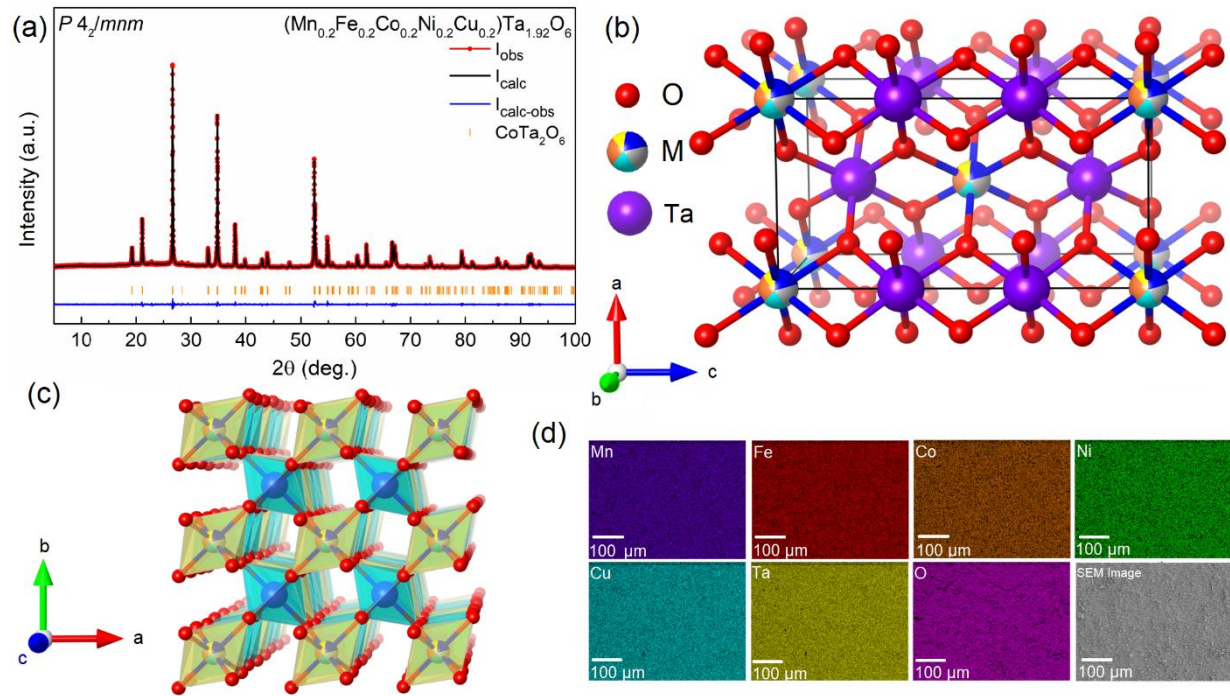


Figure 1 (a) Powder XRD pattern of $(\text{Mn}_{0.2}\text{Fe}_{0.2}\text{Co}_{0.2}\text{Ni}_{0.2}\text{Cu}_{0.2})\text{Ta}_{1.92}\text{O}_6$. The observed pattern is shown by the red line with dots while the black line represents the calculated pattern. The difference between the observed and calculated pattern is shown in blue. Bragg peaks positions of CoTa_2O_6 are visualized with orange vertical bars. (b) $(\text{Mn}_{0.2}\text{Fe}_{0.2}\text{Co}_{0.2}\text{Ni}_{0.2}\text{Cu}_{0.2})\text{Ta}_{1.92}\text{O}_6$ trirutile structure viewing from the b axis. Here, “M” stands for the $3d$ transition metals in $(\text{Mn}_{0.2}\text{Fe}_{0.2}\text{Co}_{0.2}\text{Ni}_{0.2}\text{Cu}_{0.2})\text{Ta}_{1.92}\text{O}_6$. (c) $(\text{Mn}_{0.2}\text{Fe}_{0.2}\text{Co}_{0.2}\text{Ni}_{0.2}\text{Cu}_{0.2})\text{Ta}_{1.92}\text{O}_6$ viewing from the c axis with $\text{Ta}@\text{O}_6$ (cyan) and $\text{M}@\text{O}_6$ (yellow) octahedra (d) SEM-EDS elemental mapping results of Co, Cu, Fe, Mn, Ni, Ta, and O on a $\sim 0.11\text{-mm}^2$ area of pellet sample.

Short-range antiferromagnetic ordering in $(\text{Mn}_{0.2}\text{Fe}_{0.2}\text{Co}_{0.2}\text{Ni}_{0.2}\text{Cu}_{0.2})\text{Ta}_{1.92}\text{O}_6$:

$(\text{Mn}_{0.2}\text{Fe}_{0.2}\text{Co}_{0.2}\text{Ni}_{0.2}\text{Cu}_{0.2})\text{Ta}_{1.92}\text{O}_6$ was measured for the temperature dependance of magnetic susceptibility from 1.8 to 300 K under an external magnetic field of 0.1 T in a zero-field cooling mode, as shown in Figure 2. Paramagnetic behavior was seen under high temperature while a broad

peak can be observed at ~ 4 K, as discussed later. Curie-Weiss (CW) fitting was performed from 150 to 275 K according to the modified CW law:

$$\chi = \frac{C}{T - \theta_{CW}} + \chi_0$$

where χ is the magnetic susceptibility, C is a constant independent of temperature and related to the effective moment (μ_{eff}), θ_{CW} is the CW temperature and χ_0 is a constant independent of temperature and related to the core diamagnetism and temperature-independent paramagnetic contributions such as Pauli paramagnetism. The χ_0 parameter was added to CW fitting since a slightly positive curvature was noted at ~ 250 K and was fitted to be 0.00109(1) emu/Oe/mol. The resulted θ_{CW} is -19.6 (2) K, indicating antiferromagnetic (AFM) spin-spin coupling within the

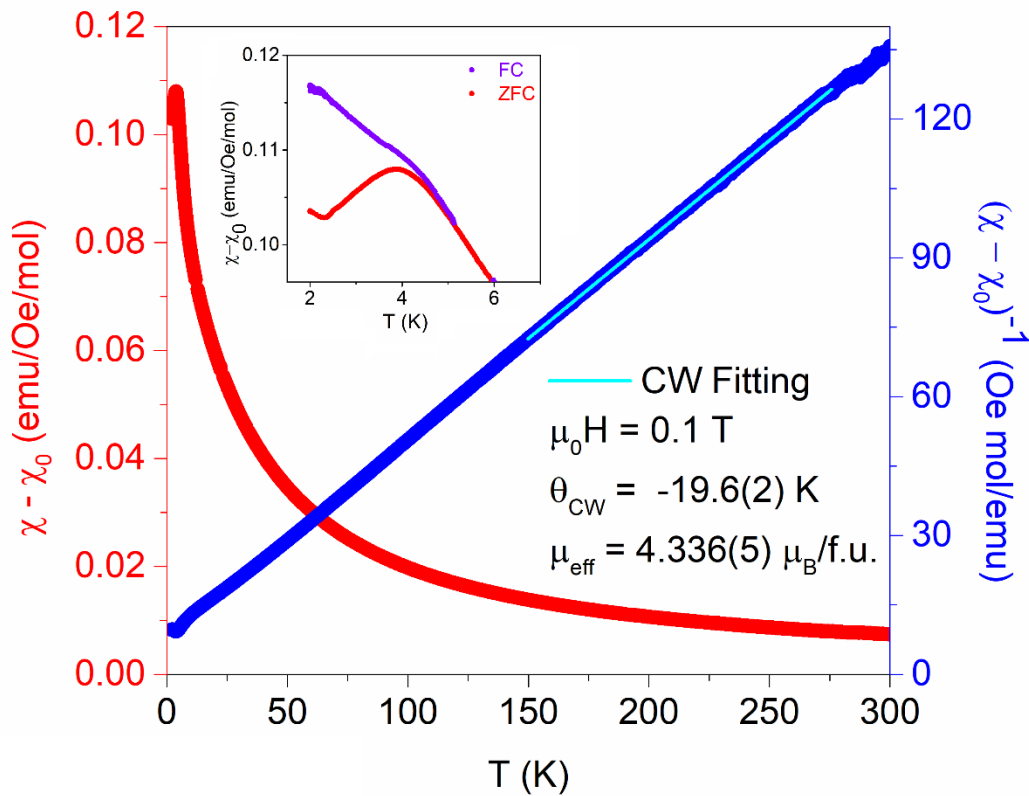


Figure 2 Magnetic susceptibility minus χ_0 (left red axis) and inverse of magnetic susceptibility minus χ_0 (right blue axis) of $(\text{Mn}_{0.2}\text{Fe}_{0.2}\text{Co}_{0.2}\text{Ni}_{0.2}\text{Cu}_{0.2})\text{Ta}_{1.92}\text{O}_6$ measured under an external magnetic field of 0.1 T with respect to temperature. The cyan line represents the Curie-Weiss fitting. The inset zooms in on the difference between the inverse of magnetic susceptibility minus χ_0 with respect to temperature under zero-field cooling (red line) and field cooling (purple line) also at an external magnetic field of 0.1 T.

fitted temperature region. Therefore, the slight deviation from CW behavior at ~ 58 K might originate from the onset of AFM coupling, as seen in Figure S1 in the SI.

Based on $\mu_{\text{eff}} (\text{spin-only}) = \sqrt{n(n+2)}$ where n is the number of unpaired electrons, the spin-only moment for all 3d transition metal ions in high-spin octahedral crystal field in our material are as follows: Mn^{2+} ($\sim 5.92 \mu_{\text{B}}$), Fe^{3+} ($\sim 5.92 \mu_{\text{B}}$), Co^{2+} ($\sim 3.88 \mu_{\text{B}}$), Ni^{2+} ($\sim 2.83 \mu_{\text{B}}$), and Cu^{2+} ($\sim 1.73 \mu_{\text{B}}$). The μ_{eff} when considering equal contributions from each 3d transition metal, averages to $\sim 4.06 \mu_{\text{B}}$ and the μ_{eff} from CW fitting was determined via $\mu_{\text{eff}} = \sqrt{8C}$ to be $4.336 (5) \mu_{\text{B}}/\text{f.u.}$, demonstrating agreement. The larger fitted μ_{eff} might be due to the unaccounted contributions from orbital angular momentum. To further demonstrate the oxidation states, XPS analysis is shown later.

As shown in Figure 2 inset, the χ vs T curve features a broad downward parabola shape at ~ 4 K when under zero-field cooling (ZFC), unlike the more linear shape that is realized under field-cooling (FC). Under low field, short range antiferromagnetic interactions exist and that leads to the broad peak; however, the feature disappears with FC due to the quenching of the minor antiferromagnetic interactions and the dominating paramagnetic state. The deviation between ZFC and FC in Figure 2 inset does not originate from a spin-glass state because for a spin glass, magnetic susceptibility would plateau at temperatures below the freezing temperature. AC magnetic susceptibility was also measured under 936 Hz, 1635 Hz and 1858 Hz from 2 K to 10 K under a DC field of 100 Oe and an AC field of 10 Oe to confirm the absence of a spin-glass state, as seen in Figure S2 in the SI. The same broad peak can be observed under ~ 5 K in Figure 2 inset, however, no shift of the peak position at different frequencies was seen. Such a behavior excludes the possibility of the spin-glass state in $(\text{Mn}_{0.2}\text{Fe}_{0.2}\text{Co}_{0.2}\text{Ni}_{0.2}\text{Cu}_{0.2})\text{Ta}_{1.92}\text{O}_6$.

The field-dependence of magnetization, as shown in Figure 3, illustrates that at 2, 10, and 300 K, $(\text{Mn}_{0.2}\text{Fe}_{0.2}\text{Co}_{0.2}\text{Ni}_{0.2}\text{Cu}_{0.2})\text{Ta}_{1.92}\text{O}_6$ does not become saturated from up to 9 T. A slightly bent feature can be seen under 2 K, which is typical for paramagnetic state. In addition, no coercive field is observed, as can be seen in Figure S3 in the SI, which can be the indicative of the absence of a long-range ordered ferromagnetic component.

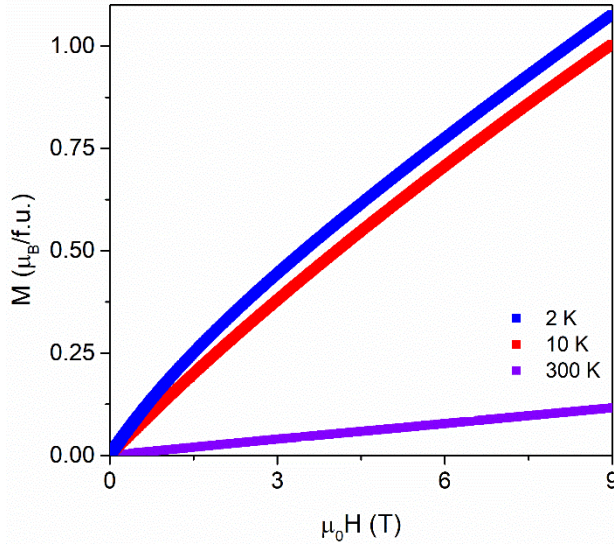


Figure 3. Field-dependent magnetization from 0-9 T at 2, 10, and 300 K, in blue, red and violet, respectively.

Heat Capacity: The temperature-dependent heat capacity of $(\text{Mn}_{0.2}\text{Fe}_{0.2}\text{Co}_{0.2}\text{Ni}_{0.2}\text{Cu}_{0.2})\text{Ta}_{1.92}\text{O}_6$ was measured from 2 to 35 K. No indication of long-range magnetic ordering, i.e., a λ -anomaly in heat capacity curve, can be seen, as shown in Figure 4(a). While a broad feature appears at ~ 4 K in Figure 4(a), Figure 4(b) plots the C_{total}/T vs T curve and the broad peak is shown at ~ 4 K. The total heat capacity of a magnetic material can be treated as the sum of electronic, phononic, and magnonic contribution where $C_{\text{total}} = C_{\text{el}} + C_{\text{ph}} + C_{\text{mag}}$. As shown by resistivity in Figure S4 in the supporting information, $(\text{Mn}_{0.2}\text{Fe}_{0.2}\text{Co}_{0.2}\text{Ni}_{0.2}\text{Cu}_{0.2})\text{Ta}_{1.92}\text{O}_6$ exhibits insulating behavior, thus there are no electronic contributions to heat capacity, i.e., $C_{\text{total}} = C_{\text{ph}} + C_{\text{mag}}$. As an estimate, $C_{\text{ph}} = \beta T^3$ according to the Debye formula where β is the vibrational contribution coefficient. However, just a T^3 term could not lead to a good fitting. Herein, T^5 , T^7 , T^9 , and T^{11} terms were added to obtain a reasonable fitting so that a polynomial fit was employed: $C_{\text{ph}}/T = \beta_1 T^2 + \beta_2 T^4 + \beta_3 T^6 + \beta_4 T^8 + \beta_5 T^{10}$ where $\beta_1, \beta_2, \beta_3, \beta_4$, and β_5 are constants and were fitted to $0.00311(9)$ J/mol/K⁴, $-8.6(5) \times 10^{-6}$ J/mol/K⁶, $1.2(1) \times 10^{-8}$ J/mol/K⁸, $-7.7(8) \times 10^{-12}$ J/mol/K¹⁰, and $2.0(2) \times 10^{-15}$ J/mol/K¹². Therefore, by subtracting the phononic contribution from C_{total}/T , pure C_{mag}/T is plotted in Figure 4(b) as blue open circles. By integrating C_{mag}/T vs T curve, the change in magnetic entropy, ΔS_{mag} , is obtained. ΔS_{mag} is usually determined by the spin multiplicity in a magnetic system where contributions from orbital angular momentum can be ignored by $\Delta S_{\text{mag}} = R \ln(2S+1)$ where R is the gas constant. Here, ΔS_{mag} does not exceed $R \ln 2$, which is the magnetic entropy change for a $S = 1/2$ system. Because

the average spin state of the 3d transition metals appearing in $(\text{Mn}_{0.2}\text{Fe}_{0.2}\text{Co}_{0.2}\text{Ni}_{0.2}\text{Cu}_{0.2})\text{Ta}_{1.92}\text{O}_6$, i.e., Mn^{2+} ($S = 5/2$), Fe^{3+} ($S = 5/2$), Co^{2+} ($S = 3/2$), Ni^{2+} ($S = 1$), and Cu^{2+} ($S = 1/2$), must be larger than $S = 3/2$. Therefore, the observed ΔS_{mag} is obviously smaller than $R\ln 4$, indicating the absence of long-range magnetic ordering within the measured temperature range in $(\text{Mn}_{0.2}\text{Fe}_{0.2}\text{Co}_{0.2}\text{Ni}_{0.2}\text{Cu}_{0.2})\text{Ta}_{1.92}\text{O}_6$. Heat capacity of $(\text{Mn}_{0.2}\text{Fe}_{0.2}\text{Co}_{0.2}\text{Ni}_{0.2}\text{Cu}_{0.2})\text{Ta}_{1.92}\text{O}_6$ was also measured under an external magnetic field, as shown in Figure S5 in the supporting information; no shift is observed for peak position. The field-independent behavior suggests that such anomaly below ~ 5 K is not spin-related, instead, it can be due to the phononic excitation.

Oxidation states of transition metal ions: XPS results shown in Figures 5(a) -5(e) highlight the 2p orbitals of each 3d transition metal ions. Observed (expected) spin orbital splitting are as follows: Mn, 11.8 eV (11.8 eV), Fe (III) 13.5 eV (14.1 eV), Co 15.3 eV (15.6 eV), Ni (II) 16.9 eV (17.5 eV), and Cu 19.8 eV (19.8 eV). Satellite peaks are present in all spectra, consistent with other reports²⁷⁻²⁹. Only one set of peaks for 2p_{3/2} and 2p_{1/2} were fitted for all transition metals, without a clear distinction of more than one oxidation state. For Mn, the peaks corresponding to 2p_{3/2} and 2p_{1/2} are at 641.0 eV and 652.8 eV, which are consistent with reported Mn^{2+} .²⁷ Similarly, the 2p_{3/2} and 2p_{1/2} peaks in the Fe (710.6 and 724.7 eV), Co (780.8 and 796.4 eV), Ni (855.8 and 873.3 eV),

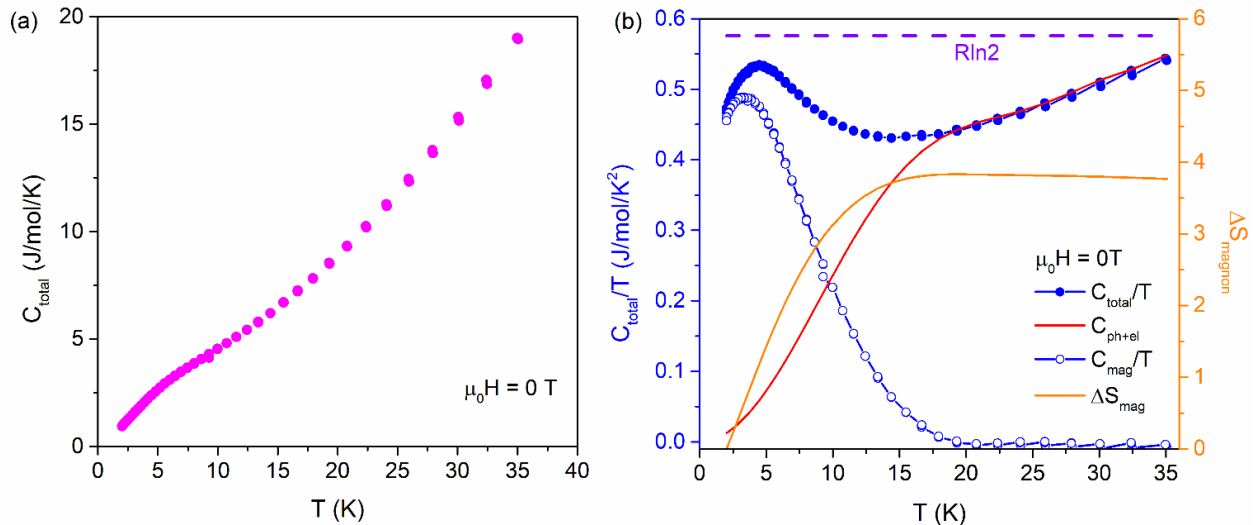


Figure 4 (a). C_{total} is shown in magenta as a function of temperature. **(b)** C_{total}/T is shown in blue filled circles while C_{mag}/T is shown in blue open circles. The fitted C_{ph} is graphed in red. These three curves correspond to the left blue axis. $R\ln 2$ is shown by the orange dashed line and ΔS_{mag} is the solid orange line; both lines correspond to the right orange axis.

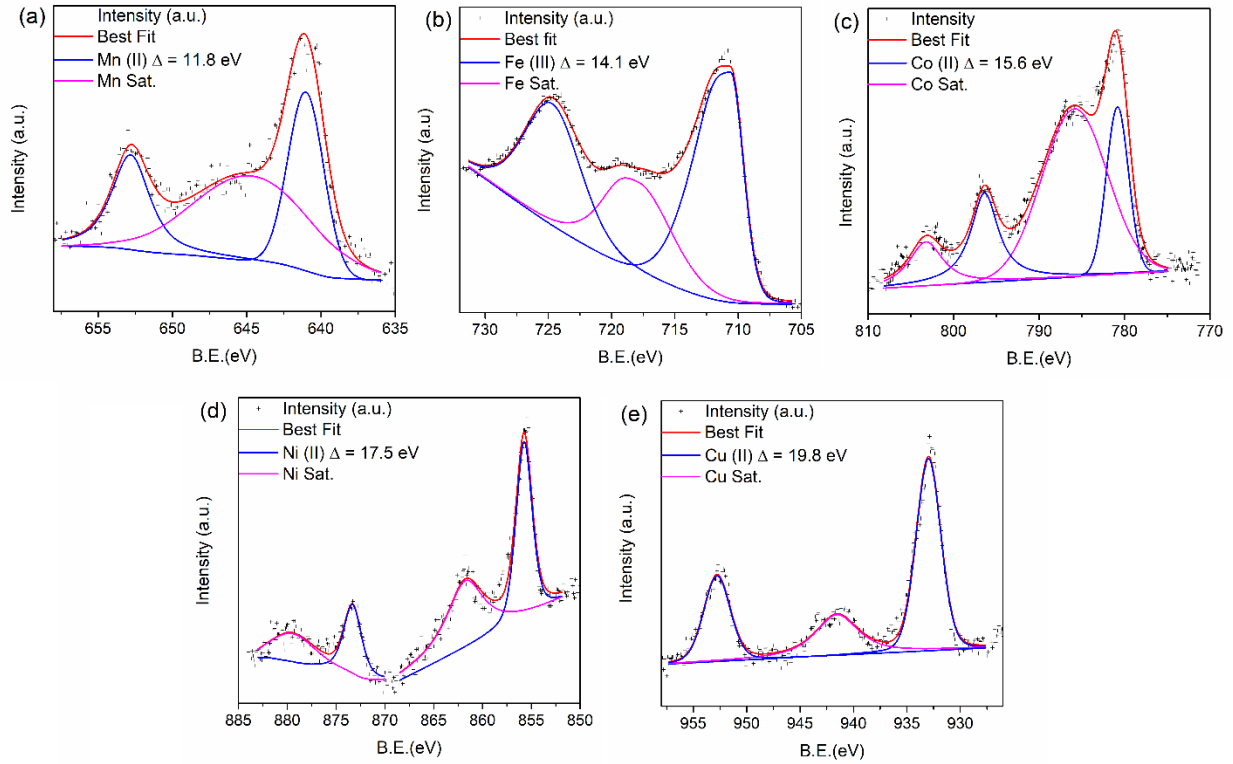


Figure 5. XPS of $(\text{Mn}_{0.2}\text{Fe}_{0.2}\text{Co}_{0.2}\text{Ni}_{0.2}\text{Cu}_{0.2})\text{Ta}_{1.92}\text{O}_6$ in range of $2p$ orbitals for (a) Mn, (b) Fe, (c) Co, (d) Ni and (e) Cu. In each graph, the line of best fit is shown in red. Pairs of peaks are shown in blue while satellite peaks are shown in magenta. B.E. stands for binding energy.

and Cu (933.0 and 952.8 eV) spectra are consistent with Fe^{3+} ,^{27,29} Co^{2+} ,²⁷ Ni^{2+} ,²⁷ and Cu^{2+} .²⁸ Therefore, the XPS results confirmed the spin states that we speculated from the magnetic data.

Magnetic superexchange interaction and possible origin of short-range magnetic ordering:

Based on the crystal structure of $(\text{Mn}_{0.2}\text{Fe}_{0.2}\text{Co}_{0.2}\text{Ni}_{0.2}\text{Cu}_{0.2})\text{Ta}_{1.92}\text{O}_6$, two possible magnetic superexchange pathways can be proposed, as illustrated in Figure 6, while the other pathways are related to them by symmetries. The atomic orbitals of $\text{M}^{2+/3+}$ near the Fermi energy are determined by the semi-empirical extended-Hückel-tight-binding (EHTB) methods and CAESAR packages, as described in the SI. The calculation was only conducted on the parent compound, CoTa_2O_6 , due to the complexities of the high-entropy $(\text{Mn}_{0.2}\text{Fe}_{0.2}\text{Co}_{0.2}\text{Ni}_{0.2}\text{Cu}_{0.2})\text{Ta}_{1.92}\text{O}_6$. However, the symmetries of molecular orbitals in CoTa_2O_6 can be well extended to $(\text{Mn}_{0.2}\text{Fe}_{0.2}\text{Co}_{0.2}\text{Ni}_{0.2}\text{Cu}_{0.2})\text{Ta}_{1.92}\text{O}_6$ regardless of addition or removal of valence electrons of $3d$ transition metal ions. Therefore, the analysis of molecular orbitals in the high-entropy compound

can be conducted based on the highest-occupied molecular orbital in CoTa_2O_6 by varying the number of electrons.

The first superexchange pathway is shown in Figure 6(a) where two M@O_6 octahedra are connected by Ta@O_6 octahedron via an axial manner. In this case, half-filled d_{xz} orbital of $\text{M}^{2+/3+}$, fully-filled p_x and p_z orbitals of O^{2-} and empty d_z^2 orbital of Ta^{5+} are present. The two $\text{M}^{2+/3+}$ ions on the opposite sides show antiferromagnetic coupling due to the following reasons: 1. due to the virtual electron hopping represented by the arrows, a pair of spins with opposite spin directions from oxygen p_z orbitals can populate the empty d_z^2 orbital of Ta^{5+} , which provides a more stable ground state; 2. the exchange energies between the spins with the same direction on p_x and p_z orbitals of O^{2-} stabilize the system as well, as indicated by the orange dashed lines in Figure 6; 3. virtual electron hopping can also occur between the p_x orbitals of O^{2-} and the half-filled d_{xz} orbital of $\text{M}^{2+/3+}$, which leads to a stable singlet state. The superexchange interaction depicted results in the antiferromagnetic coupling between the $\text{M}^{2+/3+}$ ions. Similar reasons and superexchange pattern can be found in the second pathway, shown in Figure 6(b), while the involved atomic orbitals are now the half-filled d_z^2 orbital of $\text{M}^{2+/3+}$, fully-filled p_x and p_y orbitals of O^{2-} and empty d_{xy} orbital of Ta^{5+} . In both cases, antiferromagnetic coupling between M ions is dominant.

With the analysis above, we can speculate three possible reasons of the short-range magnetic ordering observed in magnetic properties measurements:

- The existence of Ni^{2+} and Cu^{2+} leads to the lack of half-filled d_{xz} orbitals, which disables the scenario in Figure 6(a) where a half-filled d_{xz} orbital of $\text{M}^{2+/3+}$ is necessary. Subsequently, the corresponding superexchange pathway is not functional due to the lack of electron hopping and, thus, magnetic coupling is absent. Meanwhile, all the $\text{M}^{2+/3+}$ ions possess a half-filled d_z^2 orbital, which allows the superexchange interaction in Figure 6(b). Therefore, with part of the superexchange pathways disabled, long-range magnetic ordering does not exist in $(\text{Mn}_{0.2}\text{Fe}_{0.2}\text{Co}_{0.2}\text{Ni}_{0.2}\text{Cu}_{0.2})\text{Ta}_{1.92}\text{O}_6$.
- Due to the existence of Fe^{3+} , in order to maintain charge neutrality, possible removal of cations can take place as a result of ionic charge compensation mechanism. Therefore, part of the M^{2+} or Ta^{5+} sites may be vacant, leading to the interruption of the superexchange pathways and the absence of long-range magnetic ordering. The Ta^{5+} vacancy is seen in the inability to synthesis a high purity sample with non-deficient Ta_2O_5 amounts.

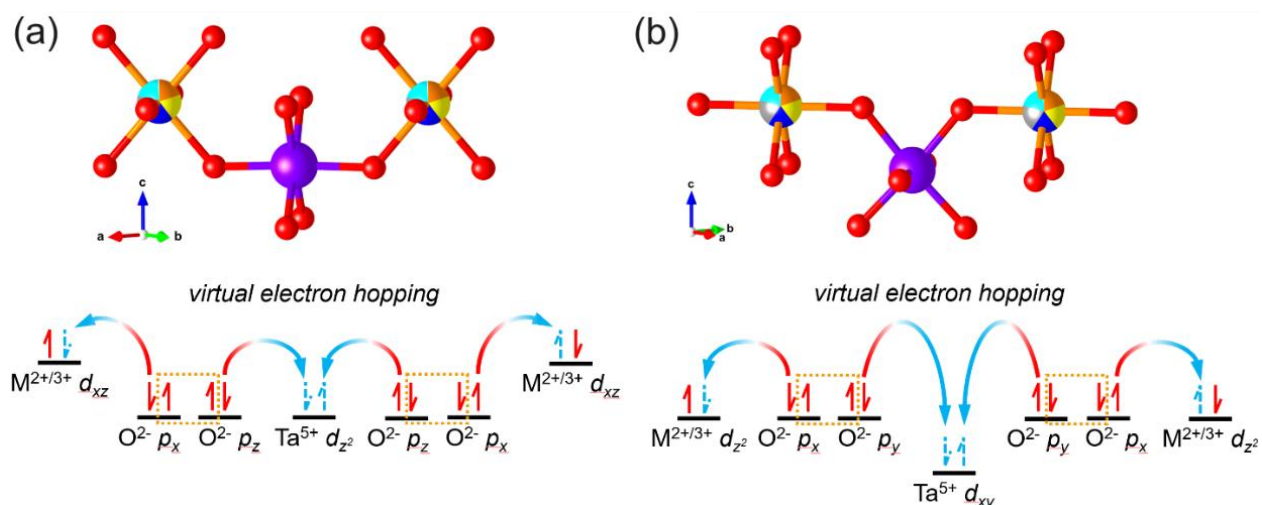


Figure 6. The two different magnetic superexchange pathways in $(\text{Mn}_{0.2}\text{Fe}_{0.2}\text{Co}_{0.2}\text{Ni}_{0.2}\text{Cu}_{0.2})\text{Ta}_{1.92}\text{O}_6$ between transition metal ions. $\text{M}^{2+/3+}$ stand for transition metal ions. The relative vertical distance between atomic orbitals stands for the relative geometry of ions. The dashed orange lines involve the pair of electrons on difference p orbitals of oxygen ions that stabilize the superexchange pathways by inclusion of exchange energy.

- The high-entropy nature of the $\text{M}^{2+/3+}$ site can result in the local distortion of the M@O_6 octahedra, which reduces the orbital overlap between $\text{M}^{2+/3+}$ and the intermediate O^{2-} . Consequently, electron hopping may not occur due to the altered symmetries of orbitals.

Conclusion

In this paper, we reported the first high-entropy oxide in a trirutile structure. High-purity phase with high configurational disorder in a uniform structure has been determined via powder XRD and EDS measurements. The new material, $(\text{Mn}_{0.2}\text{Fe}_{0.2}\text{Co}_{0.2}\text{Ni}_{0.2}\text{Cu}_{0.2})\text{Ta}_{1.92}\text{O}_6$, shows antiferromagnetic spin-spin coupling under high temperatures while exhibiting short-range antiferromagnetic ordering under low temperatures. Heat capacity further shows the evidence of the absence of long-range magnetic ordering in this compound. XPS shows the presence of divalent Mn, Co, Ni and Cu, along with trivalent Fe, which are consistent with the observation in the magnetic results. The discovery of the first trirutile high-entropy oxide builds a new platform for investigating the interplay between high-entropy nature and their magnetism. Moreover, it allows the manipulation of a wider range of physical properties in high-entropy oxides.

Associated Content

Supporting Information

The Supporting Information is available free of charge at XXX.

Deviation from Curie-Weiss behavior below ~50 K. AC magnetic susceptibility data. Magnetic hysteresis loop. Temperature-dependent resistivity data. Heat capacity data under zero and applied magnetic field. Powder XRD fitted atomic coordinates. EDS results.

Author Information

Corresponding Author: xig75@pitt.edu

Notes: The authors declare no competing financial interest.

Acknowledgements

G. A. and X.G. are supported by the startup fund from the University of Pittsburgh and the Pitt Momentum Fund. Portions of this work were performed at the Molecular Foundry and supported by the Office of Science, Office of Basic Energy Sciences, of the U.S. Department of Energy under Contract No. DE-AC02-05CH11231. Work at the University of Arizona is supported by the National Science Foundation under Award No. DMR-2338229.

References

- (1) Feng, D.; Dong, Y.; Zhang, L.; Ge, X.; Zhang, W.; Dai, S.; Qiao, Z. Holey Lamellar High-Entropy Oxide as an Ultra-High-Activity Heterogeneous Catalyst for Solvent-free Aerobic Oxidation of Benzyl Alcohol. *Angewandte Chemie* **2020**, *132* (44), 19671–19677. <https://doi.org/10.1002/ange.202004892>.
- (2) Sarkar, A.; Velasco, L.; Wang, D.; Wang, Q.; Talasila, G.; De Biasi, L.; Kübel, C.; Brezesinski, T.; Bhattacharya, S. S.; Hahn, H.; Breitung, B. High Entropy Oxides for Reversible Energy Storage. *Nat Commun* **2018**, *9* (1), 3400. <https://doi.org/10.1038/s41467-018-05774-5>.
- (3) Tyagi, P. K.; Jha, S. K. Flash Sintering Improves the Densification and Mechanical Properties of High Entropy Oxides Used in Anodic Applications. *Materialia* **2024**, *33*, 101967. <https://doi.org/10.1016/j.mtla.2023.101967>.
- (4) Ujah, C. O.; Kallon, D. V. V.; Aigbodion, V. S. Corrosion Characteristics of High-Entropy Alloys Prepared by Spark Plasma Sintering. *Int J Adv Manuf Technol* **2024**, *132* (1–2), 63–82. <https://doi.org/10.1007/s00170-024-13452-8>.
- (5) Sharma, Y.; Mazza, A. R.; Musico, B. L.; Skoropata, E.; Nepal, R.; Jin, R.; Ievlev, A. V.; Collins, L.; Gai, Z.; Chen, A.; Brahlek, M.; Keppens, V.; Ward, T. Z. Magnetic Texture in Insulating Single Crystal High Entropy Oxide Spinel Films. *ACS Appl. Mater. Interfaces* **2021**, *13* (15), 17971–17977. <https://doi.org/10.1021/acsami.1c01344>.

- (6) Rost, C. M.; Sachet, E.; Borman, T.; Moballeggh, A.; Dickey, E. C.; Hou, D.; Jones, J. L.; Curtarolo, S.; Maria, J.-P. Entropy-Stabilized Oxides. *Nat Commun* **2015**, *6* (1), 8485. <https://doi.org/10.1038/ncomms9485>.
- (7) Park, T.; Javadinejad, H. R.; Kim, Y.-K.; Chang, H. J.; Choi, H.; Woong, C.; Ashong, A. N.; Lee, Y. S.; Kim, J. H. Effect of Processing Route on the Crystal Structure and Physical Properties of Bixbyite High-Entropy Oxides. *Journal of Alloys and Compounds* **2022**, *893*, 162108. <https://doi.org/10.1016/j.jallcom.2021.162108>.
- (8) Wang, J.; Cui, Y.; Wang, Q.; Wang, K.; Huang, X.; Stenzel, D.; Sarkar, A.; Azmi, R.; Bergfeldt, T.; Bhattacharya, S. S.; Kruk, R.; Hahn, H.; Schweidler, S.; Brezesinski, T.; Breitung, B. Lithium Containing Layered High Entropy Oxide Structures. *Sci Rep* **2020**, *10* (1), 18430. <https://doi.org/10.1038/s41598-020-75134-1>.
- (9) Gild, J.; Samiee, M.; Braun, J. L.; Harrington, T.; Vega, H.; Hopkins, P. E.; Vecchio, K.; Luo, J. High-Entropy Fluorite Oxides. *Journal of the European Ceramic Society* **2018**, *38* (10), 3578–3584. <https://doi.org/10.1016/j.jeurceramsoc.2018.04.010>.
- (10) Vinnik, D. A.; Trofimov, E. A.; Zhivulin, V. E.; Zaitseva, O. V.; Gudkova, S. A.; Starikov, A. Yu.; Zherebtsov, D. A.; Kirsanova, A. A.; Häßner, M.; Niewa, R. High-Entropy Oxide Phases with Magnetoplumbite Structure. *Ceramics International* **2019**, *45* (10), 12942–12948. <https://doi.org/10.1016/j.ceramint.2019.03.221>.
- (11) Kirsch, A.; Bøjesen, E. D.; Lefeld, N.; Larsen, R.; Mathiesen, J. K.; Skjærvø, S. L.; Pittkowski, R. K.; Sheptyakov, D.; Jensen, K. M. Ø. High-Entropy Oxides in the Mullite-Type Structure. *Chem. Mater.* **2023**, *35* (20), 8664–8674. <https://doi.org/10.1021/acs.chemmater.3c01830>.
- (12) Jiang, S.; Hu, T.; Gild, J.; Zhou, N.; Nie, J.; Qin, M.; Harrington, T.; Vecchio, K.; Luo, J. A New Class of High-Entropy Perovskite Oxides. *Scripta Materialia* **2018**, *142*, 116–120. <https://doi.org/10.1016/j.scriptamat.2017.08.040>.
- (13) Li, F.; Zhou, L.; Liu, J.-X.; Liang, Y.; Zhang, G.-J. High-Entropy Pyrochlores with Low Thermal Conductivity for Thermal Barrier Coating Materials. *J Adv Ceram* **2019**, *8* (4), 576–582. <https://doi.org/10.1007/s40145-019-0342-4>.
- (14) Jiang, B.; Bridges, C. A.; Unocic, R. R.; Pitike, K. C.; Cooper, V. R.; Zhang, Y.; Lin, D.-Y.; Page, K. Probing the Local Site Disorder and Distortion in Pyrochlore High-Entropy Oxides. *J. Am. Chem. Soc.* **2021**, *143* (11), 4193–4204. <https://doi.org/10.1021/jacs.0c10739>.
- (15) Dąbrowa, J.; Adameczyk, J.; Stępień, A.; Zajusz, M.; Bar, K.; Berent, K.; Świerczek, K. Synthesis and Properties of the Gallium-Containing Ruddlesden-Popper Oxides with High-Entropy B-Site Arrangement. *Materials* **2022**, *15* (18), 6500. <https://doi.org/10.3390/ma15186500>.
- (16) Johnstone, G. H. J.; González-Rivas, M. U.; Taddei, K. M.; Sutarto, R.; Sawatzky, G. A.; Green, R. J.; Oudah, M.; Hallas, A. M. Entropy Engineering and Tunable Magnetic Order in the Spinel High-Entropy Oxide. *J. Am. Chem. Soc.* **2022**, *144* (45), 20590–20600. <https://doi.org/10.1021/jacs.2c06768>.

- (17) Witte, R.; Sarkar, A.; Kruk, R.; Eggert, B.; Brand, R. A.; Wende, H.; Hahn, H. High-Entropy Oxides: An Emerging Prospect for Magnetic Rare-Earth Transition Metal Perovskites. *Phys. Rev. Materials* **2019**, *3* (3), 034406. <https://doi.org/10.1103/PhysRevMaterials.3.034406>.
- (18) Yin, Y.; Shi, F.; Liu, G.-Q.; Tan, X.; Jiang, J.; Tiwari, A.; Li, B. Spin-Glass Behavior and Magnetocaloric Properties of High-Entropy Perovskite Oxides. *Applied Physics Letters* **2022**, *120* (8), 082404. <https://doi.org/10.1063/5.0081688>.
- (19) Yu, Y.; Liu, S.; Wang, H.; Zhang, S.; Wang, N.; Jiang, W.; Liu, C.; Ding, W.; Zhang, Z.; Dong, C. Synthesis and Optoelectrical Properties of $\text{Ti}_8\text{Sn}_8\text{Nb}_8\text{Ta}_8\text{Me}_{16}\text{O}_{96}$ (Me=Ga, Fe) Rutile Structure High Entropy Oxides. *Vacuum* **2022**, *203*, 111315. <https://doi.org/10.1016/j.vacuum.2022.111315>.
- (20) Law, J. M.; Koo, H.-J.; Whangbo, M.-H.; Brücher, E.; Pomjakushin, V.; Kremer, R. K. Strongly Correlated One-Dimensional Magnetic Behavior of NiTa_2O_6 . *Phys. Rev. B* **2014**, *89* (1), 014423. <https://doi.org/10.1103/PhysRevB.89.014423>.
- (21) Golubev, A.; Dinnebier, R. E.; Schulz, A.; Kremer, R. K.; Langbein, H.; Senyshyn, A.; Law, J. M.; Hansen, T. C.; Koo, H.-J.; Whangbo, M.-H. Structural and Magnetic Properties of the Trirutile-Type 1D-Heisenberg Anti-Ferromagnet CuTa_2O_6 . *Inorg. Chem.* **2017**, *56* (11), 6318–6329. <https://doi.org/10.1021/acs.inorgchem.7b00421>.
- (22) Kremer, R. K.; Greedan, J. E. Magnetic Ordering in CoTa_2O_6 and NiTa_2O_6 . *Journal of Solid State Chemistry* **1988**, *73* (2), 579–582. [https://doi.org/10.1016/0022-4596\(88\)90149-1](https://doi.org/10.1016/0022-4596(88)90149-1).
- (23) Baral, R.; Fierro, H. S.; Rueda, C.; Sahu, B.; Strydom, A. M.; Poudel, N.; Gofryk, K.; Manciu, F. S.; Ritter, C.; Heitmann, T. W.; Belbase, B. P.; Bati, S.; Ghimire, M. P.; Nair, H. S. Signatures of Low-Dimensional Magnetism and Short-Range Magnetic Order in Co-Based Trirutiles. *Phys. Rev. B* **2019**, *100* (18), 184407. <https://doi.org/10.1103/PhysRevB.100.184407>.
- (24) Rodríguez-Carvajal, J. Recent Advances in Magnetic Structure Determination by Neutron Powder Diffraction. *Physica B* **1993**, *192* (1), 55–69. [https://doi.org/10.1016/0921-4526\(93\)90108-I](https://doi.org/10.1016/0921-4526(93)90108-I).
- (25) Reimers, J. N.; Greedan, J. E.; Stager, C. V.; Kremer, R. Crystal Structure and Magnetism in CoSb_2O_6 and CoTa_2O_6 . *Journal of Solid State Chemistry* **1989**, *83* (1), 20–30. [https://doi.org/10.1016/0022-4596\(89\)90049-2](https://doi.org/10.1016/0022-4596(89)90049-2).
- (26) Ji, Y.; Guo, H. S.; Zhong, T. X.; Zhang, H.; Quan, X. L.; Zhang, Y. Q.; Xu, X. D. Charge and Charging Compensation on Oxides and Hydroxides in Oxygen Environmental SEM. *Ultramicroscopy* **2005**, *103* (3), 191–198. <https://doi.org/10.1016/j.ultramic.2004.12.001>.
- (27) Biesinger, M. C.; Payne, B. P.; Grosvenor, A. P.; Lau, L. W. M.; Gerson, A. R.; Smart, R. St. C. Resolving Surface Chemical States in XPS Analysis of First Row Transition Metals, Oxides and Hydroxides: Cr, Mn, Fe, Co and Ni. *Applied Surface Science* **2011**, *257* (7), 2717–2730. <https://doi.org/10.1016/j.apsusc.2010.10.051>.

(28) Biesinger, M. C.; Lau, L. W. M.; Gerson, A. R.; Smart, R. St. C. Resolving Surface Chemical States in XPS Analysis of First Row Transition Metals, Oxides and Hydroxides: Sc, Ti, V, Cu and Zn. *Applied Surface Science* **2010**, 257 (3), 887–898. <https://doi.org/10.1016/j.apsusc.2010.07.086>.

(29) Yamashita, T.; Hayes, P. Analysis of XPS Spectra of Fe²⁺ and Fe³⁺ Ions in Oxide Materials. *Applied Surface Science* **2008**, 254 (8), 2441–2449. <https://doi.org/10.1016/j.apsusc.2007.09.063>.

Supporting Information

Absence of Long-Range Magnetic Ordering in a Trirutile High-Entropy Oxide



Gina Angelo,^a Liana Klivansky,^b Jeremy G. Philbrick,^c Tai Kong,^{c,d} Jian Zhang,^b Xin Gui^{a}*

^a Department of Chemistry, University of Pittsburgh, Pittsburgh, PA, 15260, USA

^b The Molecular Foundry, Lawrence Berkeley National Laboratory, Berkeley, CA, 94720, USA

^c Department of Physics, University of Arizona, Tucson, AZ, 85721, USA

^d Department of Chemistry and Biochemistry, University of Arizona, Tucson, AZ, 85721, USA

Table of Contents

<u>Table S1</u>	2
<u>Table S2</u>	2
<u>Figure S1</u>	3
<u>Figure S2</u>	4
<u>Figure S3</u>	5
<u>Figure S4</u>	6
<u>Figure S5</u>	7

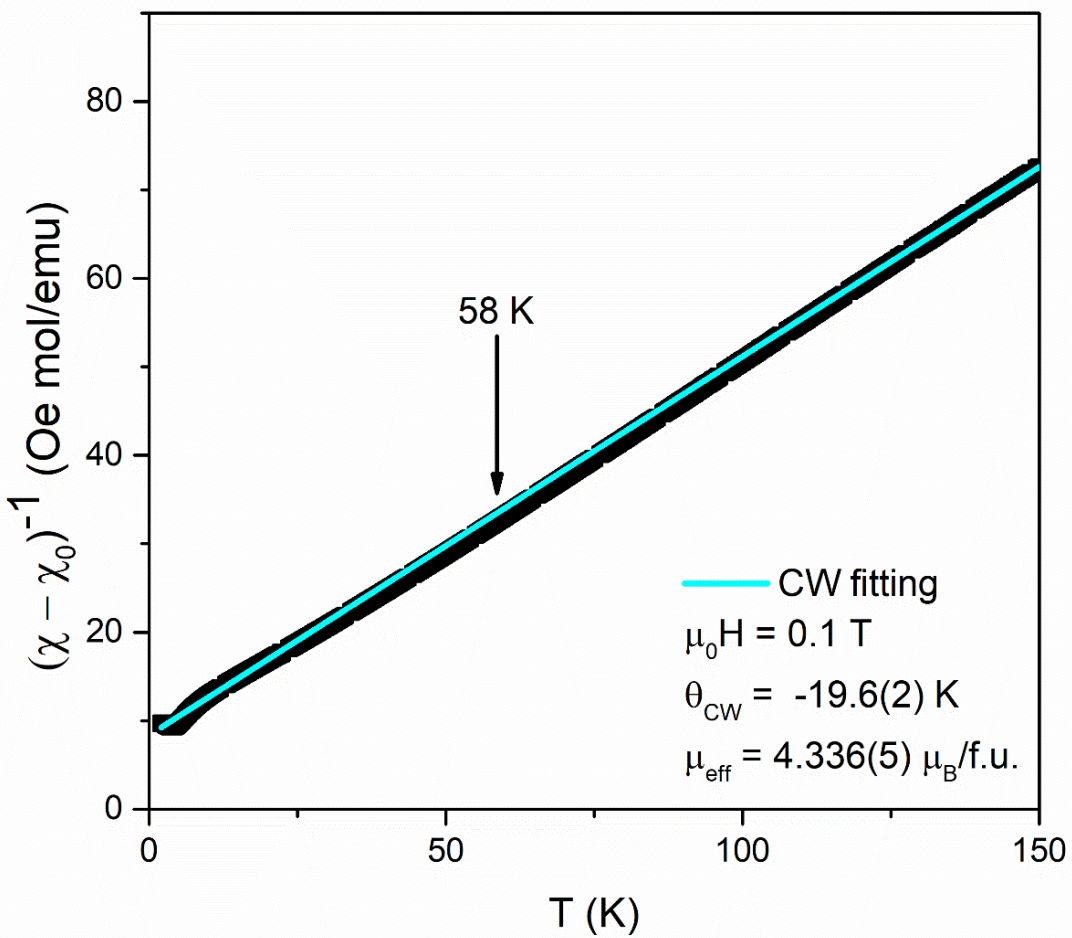


Figure S1. Deviation from the Curie-Weiss (CW) behavior at low temperatures.

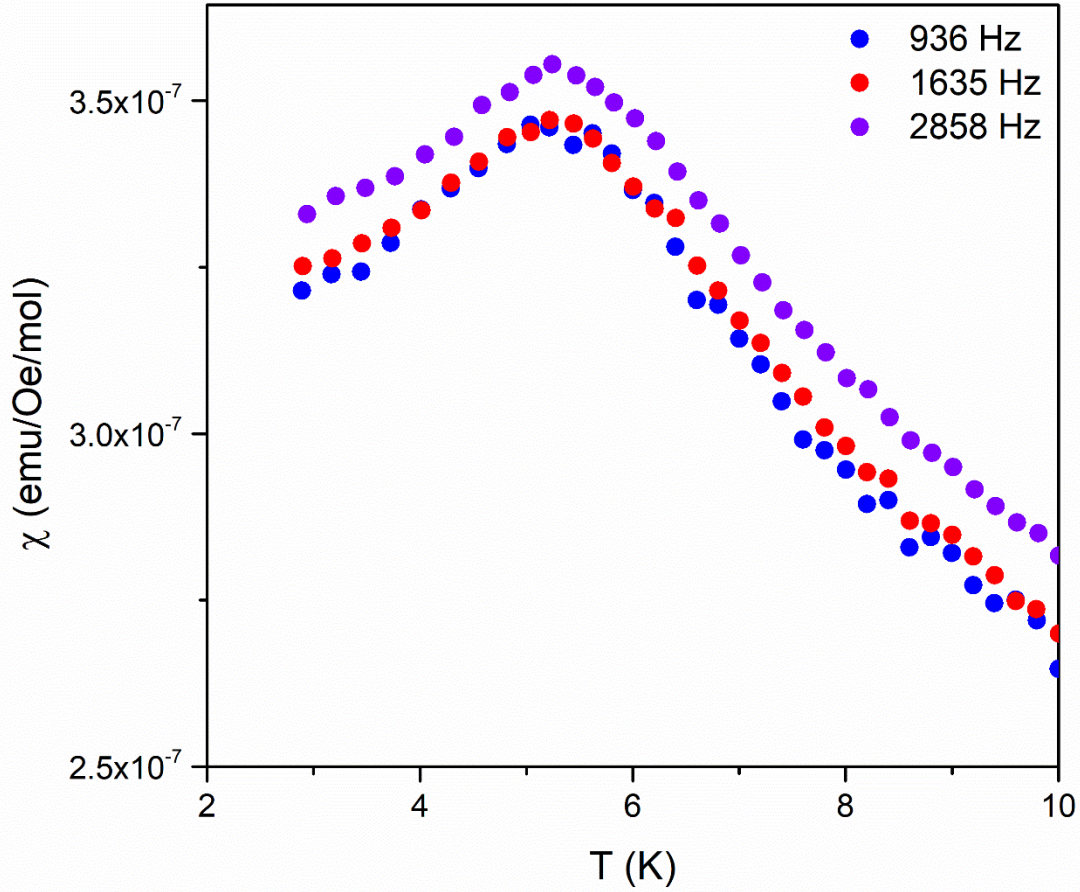


Figure S2. AC magnetic susceptibility of $(\text{Mn}_{0.2}\text{Fe}_{0.2}\text{Co}_{0.2}\text{Ni}_{0.2}\text{Cu}_{0.2})\text{Ta}_{1.92}\text{O}_6$ under various frequencies. The applied DC magnetic field is 100 Oe and the AC field is 10 Oe.

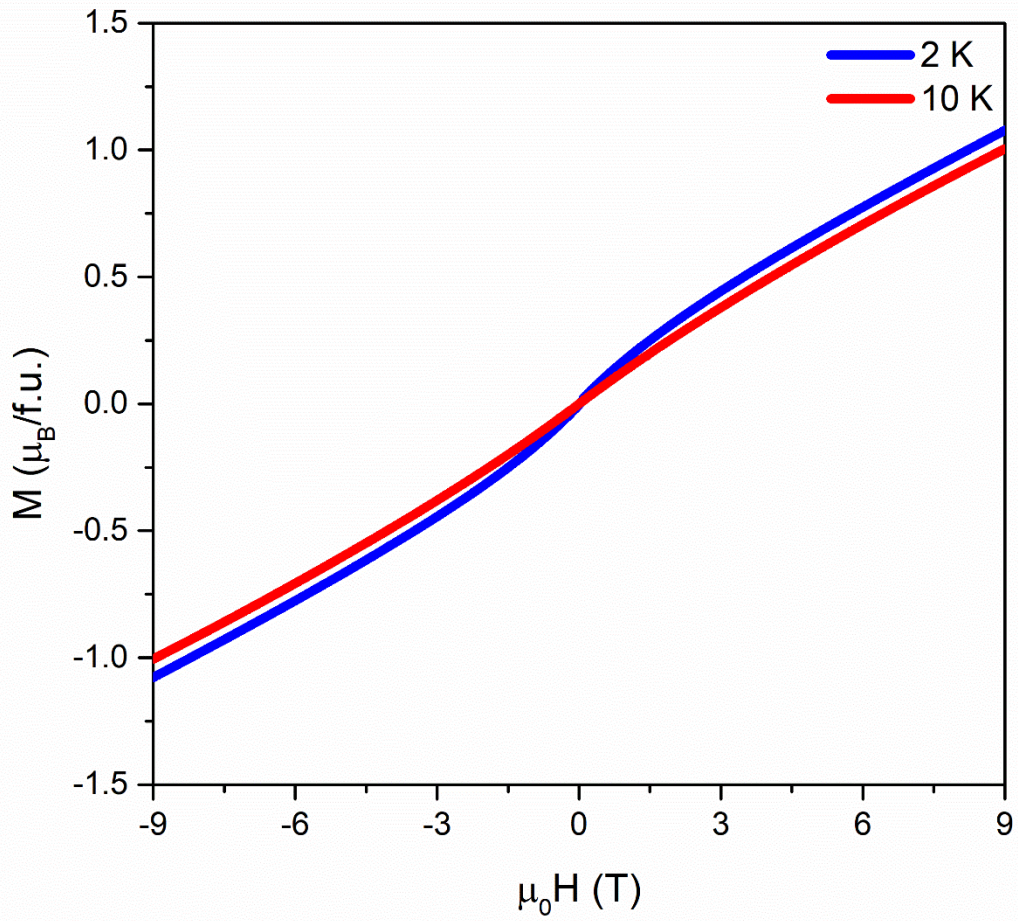


Figure S3. Hysteresis loops of $(\text{Mn}_{0.2}\text{Fe}_{0.2}\text{Co}_{0.2}\text{Ni}_{0.2}\text{Cu}_{0.2})\text{Ta}_{1.92}\text{O}_6$ at 2 K (blue) and 10 K (red).

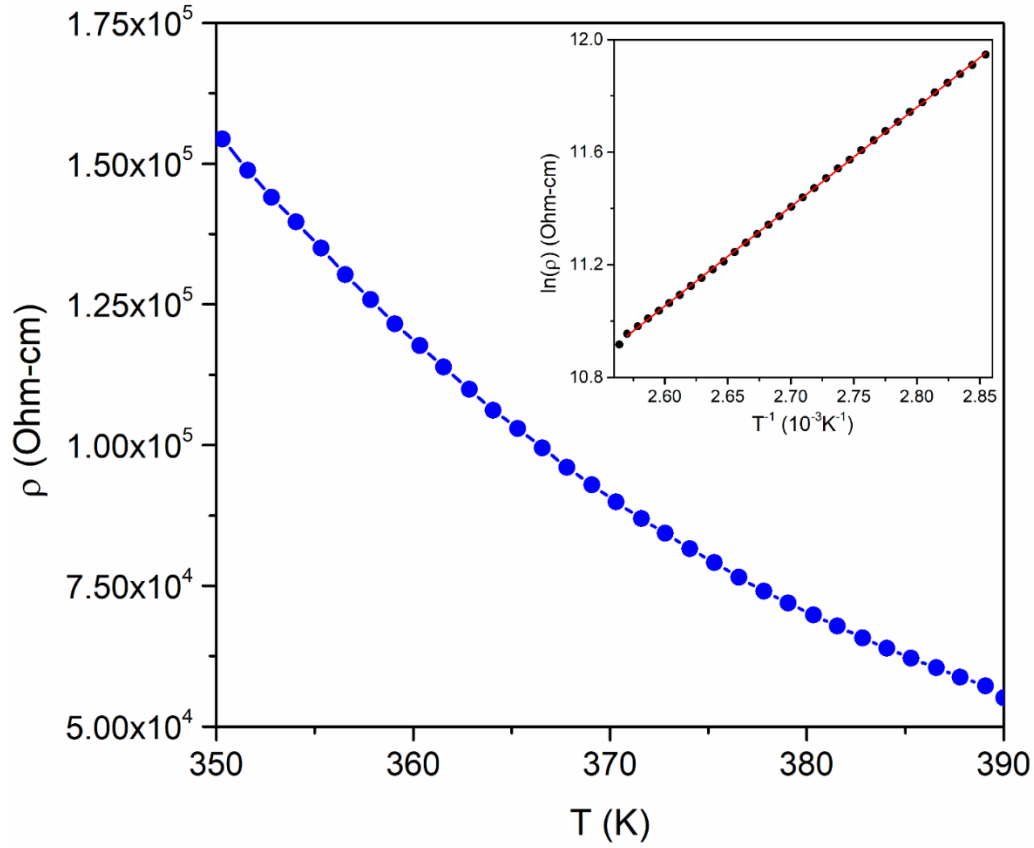


Figure S4. Resistivity of $(\text{Mn}_{0.2}\text{Fe}_{0.2}\text{Co}_{0.2}\text{Ni}_{0.2}\text{Cu}_{0.2})\text{Ta}_{1.92}\text{O}_6$ from 350 K to 390K displaying insulating behavior. The inset graph is of the linear relationship between $\ln(\rho)$ and T^{-1} . To calculate the electronic bandgap (E_g), the Arrhenius equation $\rho = \rho_0 e^{E_g/2k_B T}$, where ρ_0 is the pre-exponential term constant and k_B is Boltzmann's constant, was used. E_g was determined to be 608(1) meV.

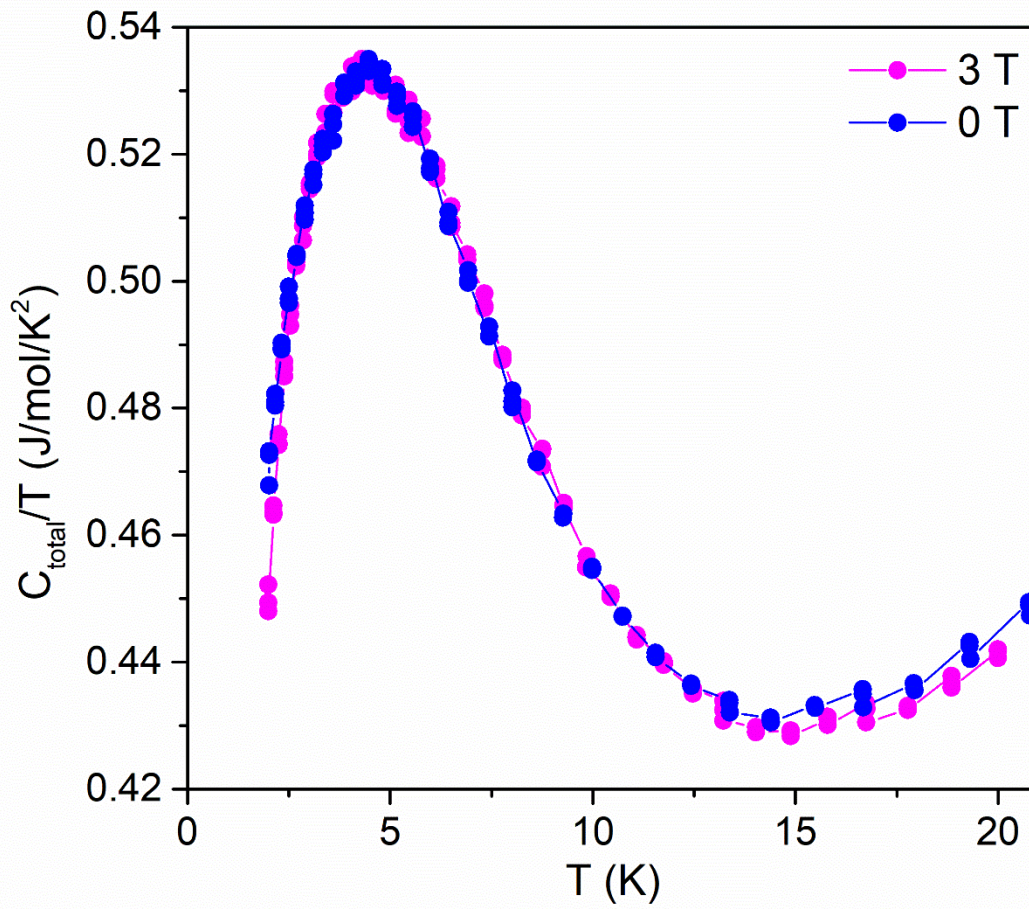


Figure S5. Temperature-dependent heat capacity of $(\text{Mn}_{0.2}\text{Fe}_{0.2}\text{Co}_{0.2}\text{Ni}_{0.2}\text{Cu}_{0.2})\text{Ta}_{1.92}\text{O}_6$ measured under magnetic field $\mu_0H = 0$ T and 3 T.

Molecular Orbital (MO) Calculation: Semi-empirical extended-Hückel-tight-binding (EHTB) methods and CAESAR packages are used in calculating molecular orbitals of the parent compound, CoTa_2O_6 .¹ The basis sets for Co are: $4s$: $H_{ii} = -9.21$ eV, $\zeta_1 = 2$, coefficient1 = 1.0000; $4p$: $H_{ii} = -5.29$ eV, $\zeta_1 = 2$, coefficient1 = 1.000; $3d$: $H_{ii} = -13.18$ eV, $\zeta_1 = 5.55$, coefficient1 = 0.568, $\zeta_2 = 2.1$, coefficient2 = 0.606. For Ta: $6s$: $H_{ii} = -10.1$ eV, $\zeta_1 = 2.28$, coefficient1 = 1.000; $6p$: $H_{ii} = -6.86$ eV, $\zeta_1 = 2.241$, coefficient1 = 1.000; $5d$: $H_{ii} = -12.1$ eV, $\zeta_1 = 4.762$, coefficient1 = 0.6815, $\zeta_2 = 1.938$, coefficient2 = 0.5589. For O: $2s$: $H_{ii} = -32.29999$ eV, $\zeta_1 = 2.275$, coefficient1 = 1.000; $2p$: $H_{ii} = -14.8$ eV, $\zeta_1 = 2.275$, coefficient1 = 1.000.

Reference

1. Hoffmann, R. An extended Hückel theory. I. hydrocarbons. *J. Chem. Phys.* **1963**, *39*, 1397-1412.